Nanoscale

PAPER

View Article Online
View Journal | View Issue

Cite this: *Nanoscale*, 2017, **9**, 2246

Near-room-temperature Chern insulator and Dirac spin-gapless semiconductor: nickel chloride monolayer

Junjie He,[a] Xiao Li,*[b] Pengbo Lyu[a] and Petr Nachtigall*[a]

A great obstacle for practical applications of the quantum anomalous Hall (QAH) effect is the lack of suitable QAH materials (Chern insulators) with a large non-trivial band gap, room-temperature magnetic order and high carrier mobility. Based on first-principles calculations it is shown here that a nickel chloride ($NiCl_3$) monolayer has all these characteristics. Thus, the $NiCl_3$ monolayer represents a new class of Dirac materials with Dirac spin-gapless semiconducting properties and high-temperature ferromagnetism (~400 K). Taking into account the spin–orbit coupling, the $NiCl_3$ monolayer becomes an intrinsic Chern insulator with a large non-trivial band gap of ~24 meV, corresponding to an operating temperature as high as ~280 K at which the quantum anomalous Hall effect could be observed. The calculated large non-trivial gap, high Curie temperature and single-spin Dirac states reported herein for the $NiCl_3$ monolayer led us to propose that this material gives a great promise for potential realization of a near-room temperature QAH effect and potential applications in spintronics. Last but not least the calculated Fermi velocities of Dirac fermions of about 4×10^5 m s^{-1} indicate very high mobility in $NiCl_3$ monolayers.

Received 31st October 2016,
Accepted 7th January 2017

DOI: 10.1039/c6nr08522a

rsc.li/nanoscale

1. Introduction

A Chern insulator or quantum anomalous Hall insulator is a novel topological phase of matter characterized by a finite Chern number and helical edge electron states within the bulk band gap.[1] Without an external magnetic field, the internal magnetic exchange interaction (ferromagnetic or antiferromagnetic order) can break time-reversal symmetry (TRS) while opening a non-trivial spin–orbital coupling induced gap, giving rise to a quantized anomalous Hall conductivity.[2] The helical edge states are robust against defects and impurities and, thus, such materials are attractive for applications in low power consumption electronic and spintronic devices.[2] Introducing magnetic order to break the TRS in topological insulators (TIs), such as chromium-doped Bi_2Te_3,[3] manganese doped HgTe quantum wells (QWs)[4] *etc.*, is expected to be a promising route for realizing the quantum anomalous Hall (QAH) effect. Very recently, the QAH effect has been observed experimentally in the topological insulator Cr doped $(Bi,Sb)_2Te_3$ film[5] at an extremely low temperature (below 30 mK) due to only a weak magnetic coupling and a corresponding small band gap. For practical applications it is crucial to search for QAH materials with a sizeable band gap, high Curie temperature (T_c), as well as a high carrier mobility.[6] Recently, a variety of QAH materials have been predicted based on impurities,[3,4,7] adatoms,[8,9] or chemical decorations[10] of graphene-like and Bi-based materials, and also in metal–organic-frameworks,[11,12] interface structures[13,14] and heterostructure materials (*i.e.* CrO_2/TiO_2, $(Bi,Sb)_2Te_3/GdI_2$, and double perovskites).[15–17] Most of these theoretically proposed materials show the QAH effect below the room-temperature T_c due to a weak magnetic order or a small spin–orbit coupling (SOC) gap.

Spin-gapless semiconductors (SGSs), exhibiting a band gap in one of the spin channels and a zero band gap in the other, have received considerable attention lately due to their unique electronic properties and potential applications in novel spintronic devices.[18] The Dirac spin-gapless semiconductors with half semi-Dirac states are based on a combination of single-spin massless Dirac fermions and half-semimetal with broken TRS. Such materials are particularly suitable for utilization of their electronic spin degrees in electronic devices.[19–22] Accounting for SOC, the gap opening may trigger QAH insulator transition in one spin channel only, which has been predicted for a few systems, such as transition-metal intercalated epitaxial graphene on SiC(0001),[17] and CrO_2/TiO_2 heterostructures.[14] The search for a new member of the Dirac SGS family with the QAH effect is of great importance for both fundamental interest and practical applications.

[a]*Department of Physical and Macromolecular Chemistry, Faculty of Science, Charles University in Prague, 128 43 Prague 2, Czech Republic. E-mail: lixiao150@gmail.com, petr.nachtigall@natur.cuni.cz*
[b]*Department of Physics, University of Texas at Austin, Austin, TX, USA*

Transition metal trichlorides ($TMCl_3$), a family of layered materials with the general formula $TMCl_3$ have unique electronic and magnetic properties.[23–28] Among them, relatively weakly interacting layers of a 3D $RuCl_3$ (dominated by van der Waals interactions) have been exfoliated into 2D materials from the bulk phase recently[29] and the first-principles calculations demonstrate that the $RuCl_3$ monolayer is metallic. Zhou *et al.*[30] have recently indicated that the mixed metal chlorides ($NiRuCl_6$) are intrinsic half-metal antiferromagnets, which can lead towards the QAH effect with an antiferromagnetic order. Based on the first principles calculations we found that the 2D $NiCl_3$ monolayer, as another member of the TMH family, is an intrinsic Dirac spin-gapless semiconductor with a high temperature ferromagnetism. When SOC is taken into account, a large gap opening is found (24 meV at the HSE06 level), giving rise to the quantum anomalous Hall states. We further confirm that the $NiCl_3$ monolayer has nontrivial topological Dirac-gap states characterized by a Chern number of $C = -1$ and chiral edge states. The physical origin of this QAH effect is due to both the intrinsic SOC and ferromagnetism of the $NiCl_3$ monolayer.

2. Results and discussion

The structure of the $NiCl_3$ monolayer is shown in Fig. 1a. Ni atoms form a 2D honeycomb lattice and each Ni atom is bonded to six Cl atoms in an octahedral environment. Geometry optimization carried out at the PBE level gives a lattice constant of 5.966 Å (Fig. 1b) and the d_{Ni-Cl} bond length is 2.60 Å. The vertical distance between the two halide planes is calculated to be 2.93 Å. The 2D Young's modulus for the $NiCl_3$ monolayer is calculated as:

$$Y_{2D} = A_0\left(\frac{\partial^2 E}{\partial A^2}\right)_{A_0} = \frac{1}{2\sqrt{3}}\left(\frac{\partial^2 E}{\partial a^2}\right)_{a_0}, \quad (1)$$

where E is the total energy of the $NiCl_3$ unit cell, a and A stand for the lattice constant and surface area, respectively. Thus the calculated 2D Young's modulus 25 N m^{-1} for the $NiCl_3$ monolayer is very close to values obtained previously for V- and Cr-based chlorides[26–28] and it is about 7% of the in-plane stiffness of graphene (340 N m^{-1}).[31] The stability of the $NiCl_3$ monolayer is confirmed by phonon spectra calculations and *ab initio* molecular dynamics (AIMD) simulations (Fig. 2). We note that the phonon band has quite small imaginary frequencies (~0.02 THz) in the vicinity of the gamma point ($k \rightarrow 0$), which can be caused by the numerical inaccuracy due to the limited supercell size. Such modes are of acoustic nature and they are derived from a collective vibration mode with a long wavelength approaching infinity,[32,33] which will not significantly affect the overall structural stability of the $NiCl_3$ monolayer. Moreover, AIMD calculations carried out for 9 ps (with a time step of 3 fs) at 500 K show clearly that the structure and energy of the $NiCl_3$ monolayer are nearly unchanged (Fig. 2b) suggesting that the $NiCl_3$ monolayers are thermally stable at room temperature. Most importantly, the system remains magnetic throughout the simulation with an average supercell magnetic moment of about $18\mu_B$ ($2\mu_B$ per unit cell), demonstrating that the magnetic state of $NiCl_3$ is robust at room temperature.

The spin-polarized FM ground state with a total magnetic moment of $2\mu_B$ per unit cell was found for $NiCl_3$ at 0 K. It corresponds to the $d^{4\uparrow 3\downarrow}$ spin configuration of Ni^{3+}, which can be verified by the Bader charge analysis.[34] To determine the preferred magnetic ground state structures of $NiCl_3$ systems at $T > 0$, the collinear FM and AFM states were considered. The nearest-neighbor exchange-coupling parameter J (the second and the third neighbor exchange-coupling are found to be a magnitude smaller than the nearest-neighbor) can be extracted by mapping the total energies of the systems with different magnetic structures to the Ising model:

$$H_{spin} = -\sum_{i,j} J S_i \cdot S_j, \quad (2)$$

where S is the net magnetic moment at the Ni site, i and j stand for the nearest Ni atoms. By mapping the DFT energies

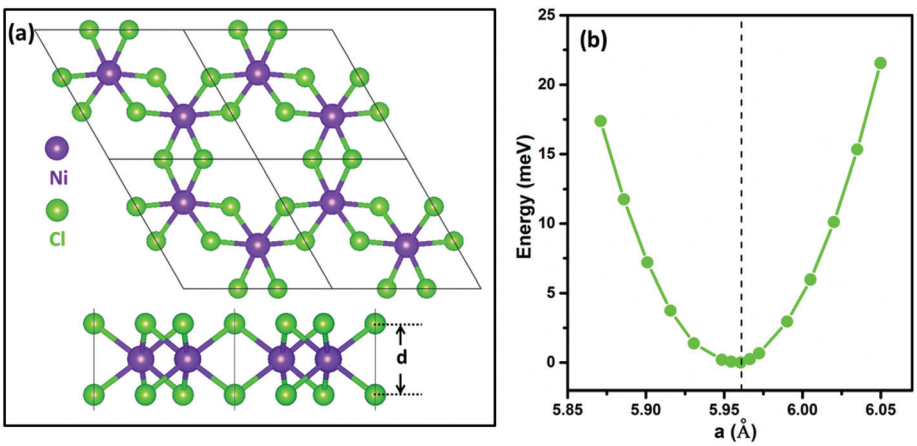

Fig. 1 (a) The top and the side views of the optimized $NiCl_3$ monolayer. (b) Variation of total energy with the lattice constant.

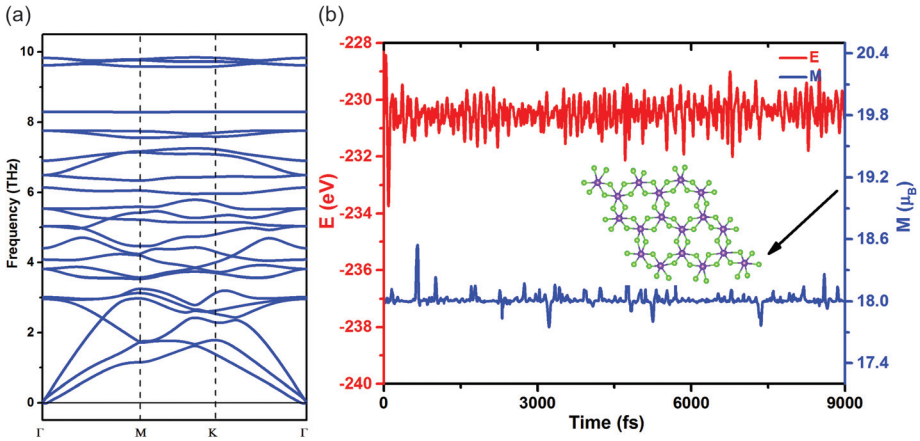

Fig. 2 (a) Phonon band structure; (b) potential energy (E) and total magnetic moment (M) fluctuations of $NiCl_3$ as a function of simulation time (depicted in red and blue, respectively). The inset shows the corresponding structure at 500 K after the simulation for 9 ps.

to the Heisenberg model, J can be calculated as $J = \Delta E/6S^2$, where ΔE is the energy difference between the ferromagnetic and antiferromagnetic order, leading to the exchange coupling parameter of 89.6 meV.

The Curie temperature T_C is a key parameter for realization of the high temperature QAH effect and for spintronic applications. Based on the Weiss molecular-field theory (MFT), T_C can be simply estimated as:

$$T_C = \frac{2zJS(S+1)}{3k_B}, \quad (3)$$

where $z = 3$ is the number of the nearest-neighbor Ni atoms in the $NiCl_3$ monolayer, and k_B is the Boltzmann constant. Thus the calculated T_C = 520 K is possibly overestimated, therefore, MC simulations based on the Ising model were also carried out. The MC simulations were performed on an 80 × 80 2D honeycomb lattice using 10^8 steps for each temperature. The temperature dependence of specific heat capacity and magnetic moments (Fig. 3) shows that the magnetic moment decreases to $0.8\mu_B$ at about 390 K and becomes $0\mu_B$ at 400 K. Therefore, the T_C value for $NiCl_3$ monolayers is estimated to be about 400 K, orders of magnitude higher than temperature for the experimentally observed QAH effect. We propose that the $NiCl_3$ monolayers can be a potential candidate for the high temperature QAH effect in spintronic applications.

The band structure of the $NiCl_3$ FM ground state is shown in Fig. 4. The spin-down channels of $NiCl_3$ possess a 1.22 eV and 4.09 eV band gap at PBE and HSE06 levels, respectively, whereas the spin-up channel shows a gapless semiconductor feature with a linear dispersion relation around the Fermi level. The spin-polarized massless Dirac fermions are found in the spin up channels of $NiCl_3$ at the high-symmetry K point of the Brillouin zone. The electronic structure of $NiCl_3$ shows rather rare Dirac spin-gapless semiconductor characteristics that are essential for potential high-speed spin filter devices. To further investigate the distribution of the linear dispersion relation in the Brillouin zone, the corresponding three dimensional band structures are also presented (Fig. 4c).

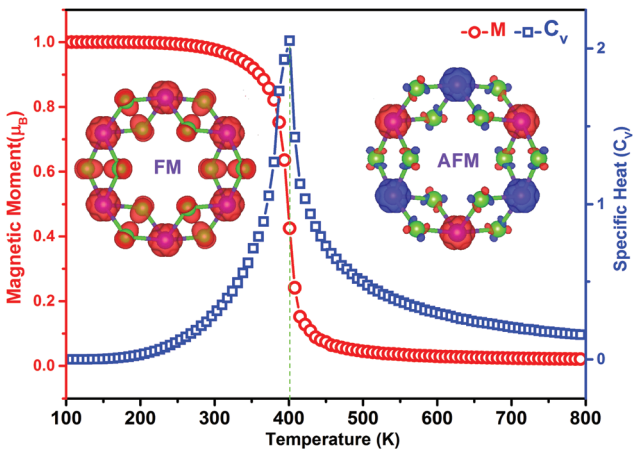

Fig. 3 Variations of the average magnetic moment (red) and specific heat (blue) calculated for a $NiCl_3$ monolayer with respect to the temperature. Spin-polarized charge densities with spin directions for $NiCl_3$ are shown in insets (blue dotted areas depicts the spin up); iso-surface value of ±0.005 e Å^{-3} is shown.

The calculated Fermi velocities (v_F) of Dirac fermions are about 4×10^5 m s^{-1} for $NiCl_3$ monolayers at the HSE06 level, a value that is approximately half of that found for graphene (8×10^5 m s^{-1}).[36]

Dirac materials, such as graphene, silicene, germanene, *etc.* are characterized by Dirac states composed of p-orbitals with weak spin–orbital couplings. Thus, SOC opens just a small gap, making these materials the Z2 topological insulators with TRS protected edged states. However, the Dirac states of $NiCl_3$ are mainly derived from the Ni-d orbitals. The larger SOC gap of Ni-d orbitals with the broken TRS may lead to the Chern insulator and QAH effect. The SOC gap was calculated by relativistic PBE + SOC calculations to be 7 meV (Fig. 4). However, SOC gaps calculated at the HSE06 level are considered more reliable and they are often comparable with experimental values. The HSE06 + SOC calculations show the 24 meV gap which is sufficiently large for the QAH effect to be operative at

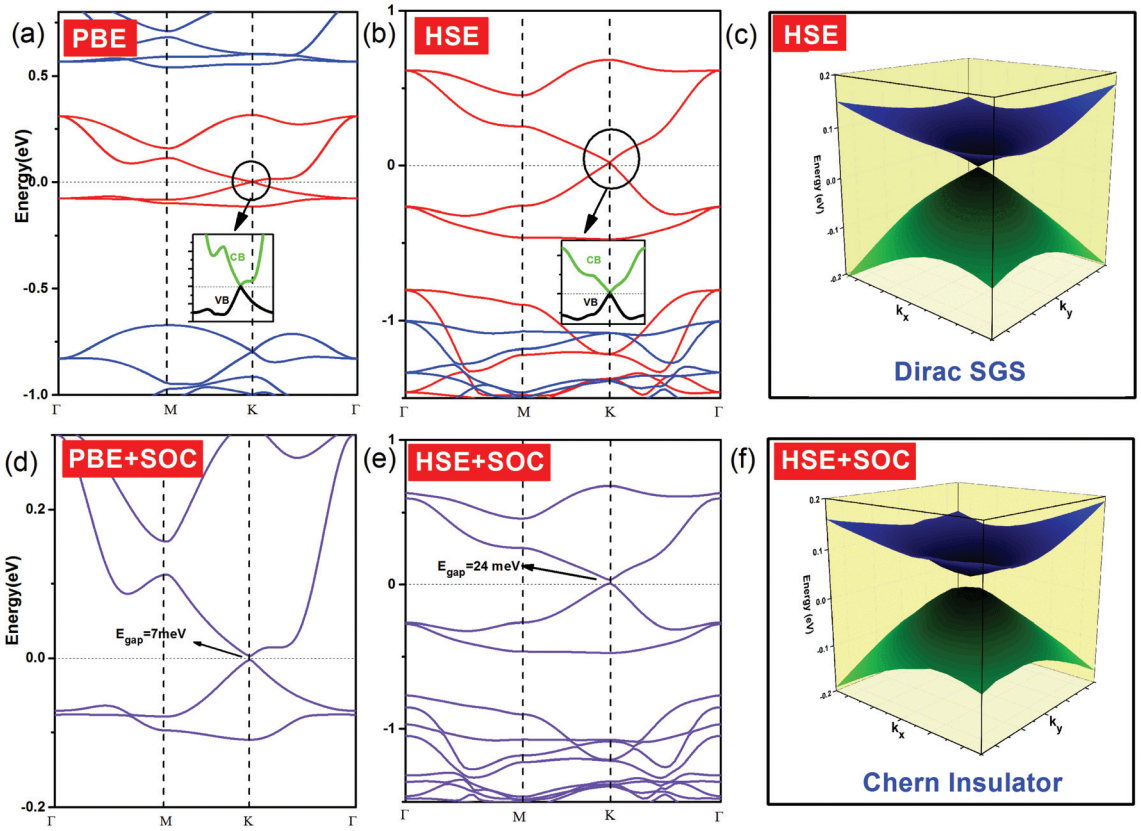

Fig. 4 Band structures of 2D $NiCl_3$ with and without SOC calculated at the PBE and HSE levels. Details of Dirac states near the Fermi level are shown in the insets of parts a and b where VB and CB are marked by green and black, respectively. The horizontal dotted lines indicate the Fermi level. The red and blue lines represent the spin up and spin down channels, respectively. The 3D band structures around the Fermi level in the 2D k space obtained without (c) and with (f) SOC are also presented.

the temperature as high as 280 K. The Chern insulator states of the $NiCl_3$ monolayer can be confirmed by the non-zero Chern numbers (C) calculated from the k-space integral of the Berry curvature ($\Omega(\vec{k})$) of all the states below the Fermi level using the formula of Kubo:[35–37]

$$C = \frac{1}{2\pi}\int_{BZ} \Omega(\vec{k}) d^2k \quad (4)$$

$$\Omega(k) = \sum_{n<E_F}\sum_{m\neq n} 2\mathrm{Im}\frac{\langle\psi_{n\vec{k}}|\nu_x|\psi_{n\vec{k}}\rangle\langle\psi_{n\vec{k}}|\nu_y|\psi_{n\vec{k}}\rangle}{(\varepsilon_{m\vec{k}}-\varepsilon_{n\vec{k}})^2}. \quad (5)$$

$\psi_{n\vec{k}}$ is the spinor Bloch wave function of band n with the corresponding eigenenergy $\varepsilon_{n\vec{k}}$. ν_x and ν_y are the i-th Cartesian components of the velocity operator.

The Berry curvature $\Omega(\vec{k})$ along the high-symmetry direction (M'–K'–Γ–K–M) has two sharp spikes of the same sign located at the K and K' points as shown in Fig. 5a. By integrating the Berry curvature in the entire Brillouin zone, the calculated Chern number C is −1 with a non-trivial topological state. As expected from the non-zero Chern number, the anomalous Hall conductivity shows a quantized charge Hall plateau of $\sigma_{xy} = Ce^2/h$ when the Fermi level is located in the insulating gap of the spin-up Dirac cone.

The existence of topologically protected chiral edge states is one of the most important consequences of the QAH state. To further reveal the nontrivial topological nature of the $NiCl_3$ monolayer, we calculate the edge states of the $NiCl_3$ monolayer with zigzag and armchair insulators using Green's functions based on Wannier functions obtained from PBE calculations, which reduces the cost of calculations while it does not change the topology of the electronic structure, besides a smaller band of 7 meV. As shown in Fig. 5, the nontrivial edge states (dark line) connecting the valence and conduction bands cross the insulating gap of the Dirac cone. The appearance of only one chiral edge state is consistent with the calculated Chern number C = −1, confirming the nontrivial topological nature of the $NiCl_3$ monolayer. The calculated gap of 24 meV corresponds roughly to 280 K, leading us to conclude that the QAH effect in $NiCl_3$ is expected to be robust up to 280 K. This is three orders of magnitude higher than the experimental temperature (<100 mK) at which QAH was observed for a Cr doped Bi_2Se_3 film.[5] Furthermore, the FM ordering temperature as high as 400 K for $NiCl_3$ is large enough to retain the QAH phase in the above-mentioned temperature range. The single spin Dirac fermion mediated topological properties of the $NiCl_3$ monolayer show a great potential to generate the QAH effect. Moreover, manipulation of valley

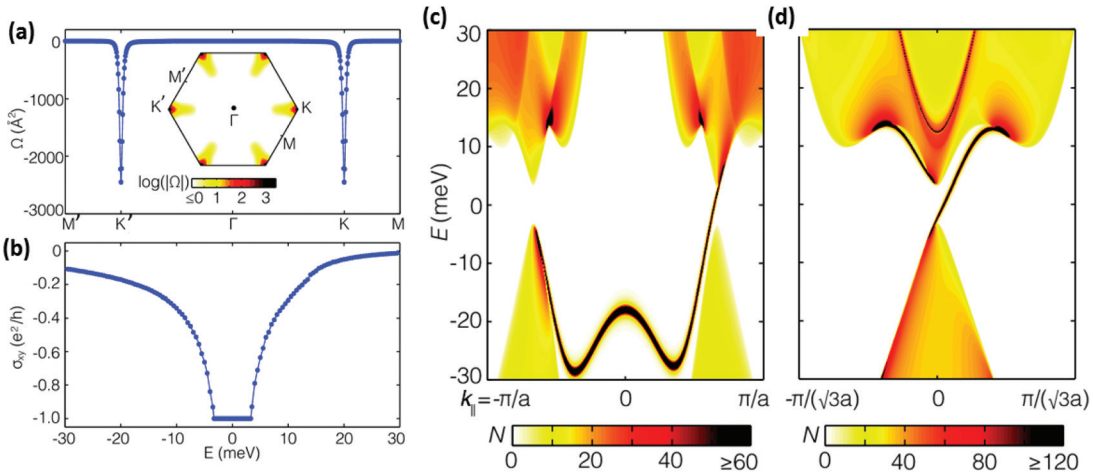

Fig. 5 (a) The distribution of the Berry curvature in momentum space for $NiCl_3$. (b) Anomalous Hall conductivity when the Fermi level is shifted from its original Fermi level. Calculated local density of states of edge states for (c) zigzag and (d) armchair insulators. The edge states are calculated on the edge of a semi-infinite plane. The warmer colors (darker) represent higher local density of states at the edge.

degrees of freedom for electrons may result in potential applications in nanoelectronic devices. The valley polarized edge states can be used as a valley filter analogous to a "spin filter".[38,39] The 2D mirror symmetry breaking in $TMCl_3$ materials leads to Rashba SOC, which may lead to the valley-polarized edge state.[40] However, Fig. 5a shows that Berry phases of two valleys are nearly identical with π contribution in each valley. The edge states in Fig. 5c connect the VB of the left valley and the CB of the right valley. Therefore, there is no observable valley-polarized edge state in $NiCl_3$. The valley-polarized edge states based on considerable Rashba SOC may be found in other $TMCl_3$ layered materials.

Finally, the PDOS and orbital-projected band structures around the Fermi level were calculated for the $NiCl_3$ monolayer to gain insight into the origin of electronic, magnetic and topological properties (Fig. 6). Under the distorted octahedral crystal field of Cl atoms, the d orbital of Ni would be split into e_1 (d_{xz}, d_{yz}), e_2 (d_{xy}, $d_{x^2-y^2}$) and a_1 (d_{z^2}) states. Based on Griffith's crystal field theory, the spin states of TM ions can be determined by the relative strength between crystal field splitting (ΔE_{cf}) and Hund exchange splitting (ΔE_{ex}) of d orbitals. The exchange splitting (0.4 eV) is smaller than the crystal field splitting (0.7 eV) for the $NiCl_3$ monolayer resulting in a low spin ($1\mu_B$) state which is in agreement with the Ni($d^{\uparrow4\downarrow3}$) spin configuration. The states near the Fermi level have main contributions from the e_1 and e_2 states in [−0.2, 0.44 eV] windows, while the a_1 state does not contribute significantly. The partially occupied e_1 and e_2 orbitals around the Fermi level form a Dirac point in the $NiCl_3$ monolayer. PDOS for e_1 and e_2 orbitals are shown in Fig. 6 together with orbital-projected band structures. The states near the Fermi level are dominated by e_2 orbitals with only a small contribution from e_1 orbitals. Without SOC, both VB and CB show an equivalent weight for e_1 and e_2 states. Calculations with SOC show significantly increased

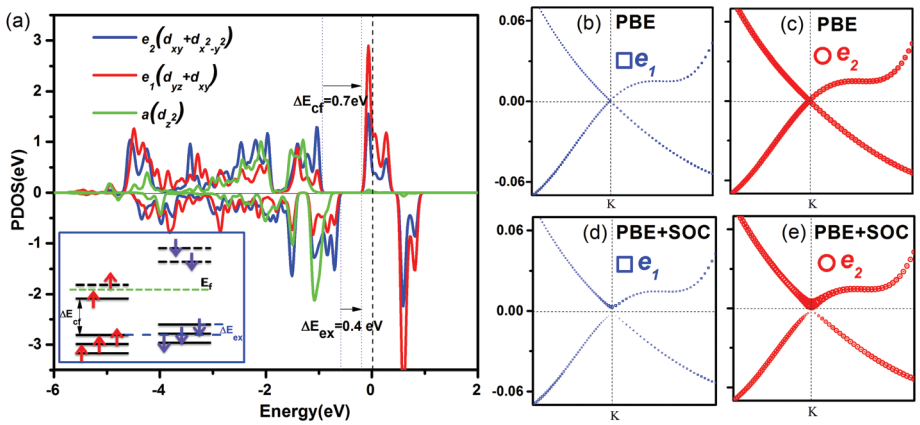

Fig. 6 (a) The PDOS of d states for Ni atoms is shown. The schematic figure (inset in part a) is the crystal field splitting and exchange splitting for Ni ions. (b) The evolution of orbital-resolved band structures (e_1 and e_2 states) of a $NiCl_3$ monolayer without and with SOC. The Fermi level is set to zero.

contributions of both e_1 and e_2 in CB while the e_1 and e_2 contributions to VB decrease. As a result, the degeneracy of e_1 levels (and similarly the degeneracy of e_2 levels) around the Dirac point is lifted, opening thus a global energy gap between CB and VB bands (Fig. 6b). The SOC results in the significant changes of e_1 and e_2 orbital energies and their contributions to CB and VB and consequently it plays a crucial role in the topological properties of the $NiCl_3$ monolayer.

3. Conclusions

DFT calculations were used in a systematic investigation of the stability, and electronic and magnetic structures of $NiCl_3$ monolayers. The thermal and dynamical stabilities have been confirmed by phonon calculations and *ab initio* molecular dynamics simulations. The $NiCl_3$ monolayers show the Dirac spin-gapless semiconducting characteristics and high-temperature ferromagnetism. The Monte Carlo simulations based on the Ising model demonstrate that the Curie temperature of the $NiCl_3$ monolayer is estimated to be as high as 400 K. In addition, a Fermi velocity (v_F) in the $NiCl_3$ monolayer is calculated to be 4×10^5 m s^{-1}, which is comparable to graphene (8×10^5 m s^{-1}). Taking the spin–orbit coupling into account, the $NiCl_3$ monolayer becomes an intrinsic Chern insulator with a large non-trivial band gap of about 24 meV, corresponding to an operating temperature of 280 K. The large non-trivial gap, high Curie temperature and single-spin Dirac states for $NiCl_3$ monolayers give rise to great expectations for both the realization of near room temperature QAH effect and potential applications in spintronics.

4. Methods and computational details

All calculations were performed using the Vienna *ab initio* simulation package (VASP)[41,42] within the generalized gradient approximation, using the Perdew–Burke–Ernzerhof (PBE) exchange–correlation functional.[43] Electronic properties (SOC in particular) were also calculated with the hybrid HSE06 functional. Interactions between electrons and nuclei were described by the projector-augmented wave (PAW) method. The criteria of energy and atom force convergence were set to 10^{-6} eV and 0.001 eV $Å^{-1}$, respectively. A plane-wave kinetic energy cutoff of 500 eV was employed. The vacuum space of 15 Å along the $NiCl_3$ normal was adopted for calculations on monolayers. The Brillouin zone (BZ) was sampled using $15 \times 15 \times 1$ gamma-centered Monkhorst–Pack grids for the calculations of relaxation and electronic structures. Furthermore, to examine the thermal stability of $NiCl_3$, the *ab initio* molecular dynamics (AIMD) simulations at 300 K were performed using the Nosé heat bath approach in a canonical ensemble. A $3 \times 3 \times 1$ supercell of the $NiCl_3$ monolayer was used in MD simulations. The phonon frequencies were calculated using a finite displacement approach as implemented in the PHONOPY code, in which a $2 \times 2 \times 1$ supercell and a displacement of 0.01 Å from the equilibrium atomic positions were employed.[44,45] The electronic properties of the $NiCl_3$ monolayer obtained by VASP have been further reproduced by the QUANTUM ESPRESSO package,[46] with the norm-conserving pseudopotentials from the PS library[47] and a 120 Ry plane wave cutoff. Based on the Wannier functions obtained from the first-principles calculations in QUANTUM ESPRESSO,[48–50] we construct the edge Green's function of the semi-infinite $NiCl_3$ monolayer. The edge spectral density of states, computed by the edge Green's function, shows the energy dispersion of edge states.[51] The Berry curvature and the anomalous Hall conductivity are also calculated by the Wannier interpolation.[49]

Acknowledgements

This work was funded by the Czech Science Foundation Grant No. P106/12/G015 and by OP VVV "Excellent Research Teams", project No. CZ.02.1.01/0.0/0.0/15_003/0000417 – CUCAM. Support by the 973 Program (Projects 2013CB921900), DOE (DE-FG03-02ER45958, Division of Materials Science and Engineering) and Welch Foundation (F-1255) is also acknowledged (XL).

References

1 F. D. M. Haldane, *Phys. Rev. Lett.*, 1988, **61**, 2015.
2 B. I. Halperin, *Phys. Rev. B: Condens. Matter*, 1982, **25**, 2185.
3 R. Yu, W. Zhang, H. J. Zhang, S. C. Zhang, X. Dai and Z. Fang, *Science*, 2010, **329**, 61–64.
4 C. X. Liu, X. L. Qi, X. Dai, Z. Fang and S. C. Zhang, *Phys. Rev. Lett.*, 2008, **101**, 146802.
5 C. Z. Chang, J. Zhang, X. Feng, J. Shen, Z. Zhang, M. Guo and Z. Q. Ji, *Science*, 2013, **340**, 167–170.
6 H. Weng, R. Yu, X. Hu, X. Dai and Z. Fang, *Adv. Phys.*, 2015, **64**, 227–282.
7 H. Jiang, Z. Qiao, H. Liu and Q. Niu, *Phys. Rev. B: Condens. Matter*, 2012, **85**, 045445.
8 H. Zhang, C. Lazo, S. Blügel, S. Heinze and Y. Mokrousov, *Phys. Rev. Lett.*, 2012, **108**, 056802.
9 J. Liu, S. Y. Park, K. F. Garrity and D. Vanderbilt, *Phys. Rev. Lett.*, 2016, **117**, 257201.
10 S. C. Wu, G. Shan and B. Yan, *Phys. Rev. Lett.*, 2014, **113**, 256401.
11 L. Dong, Y. Kim, D. Er, A. M. Rappe and V. B. Shenoy, *Phys. Rev. Lett.*, 2016, **116**, 096601.
12 Z. F. Wang, Z. Liu and F. Liu, *Phys. Rev. Lett.*, 2013, **110**, 196801.
13 H. Fu, Z. Liu, C. Lian, J. Zhang, H. Li, J. T. Sun and S. Meng, *Phys. Rev. B: Condens. Matter*, 2016, **94**, 035427.
14 K. F. Garrity and D. Vanderbilt, *Phys. Rev. B: Condens. Matter*, 2014, **90**, 121103.
15 A. M. Cook and A. Paramekanti, *Phys. Rev. Lett.*, 2014, **113**, 077203.
16 T. Cai, X. Li, F. Wang, S. Ju, J. Feng and C. D. Gong, *Nano Lett.*, 2015, **15**, 6434–6439.

17 G. Xu, J. Wang, C. Felser, X. L. Qi and S. C. Zhang, *Nano Lett.*, 2015, **15**, 2019–2023.
18 X. L. Wang, *Phys. Rev. Lett.*, 2008, **100**, 156404.
19 V. Pardo and W. E. Pickett, *Phys. Rev. Lett.*, 2009, **102**, 166803.
20 H. Ishizuka and Y. Motome, *Phys. Rev. Lett.*, 2012, **109**, 237207.
21 Y. Li, D. West, H. Huang, J. Li, S. B. Zhang and W. Duan, *Phys. Rev. B: Condens. Matter*, 2015, **92**, 201403.
22 X. L. Wang, 2016, *arXiv:1607.06057*.
23 M. A. McGuire, H. Dixit, V. R. Cooper and B. C. Sales, *Chem. Mater.*, 2015, **27**, 612–620.
24 H. Hillebrecht, P. J. Schmidt, H. W. Rotter, G. Thiele, P. Zönnchen, H. Bengel and M. H. Whangbo, *J. Alloys Compd.*, 1997, **246**, 70–79.
25 F. Hulliger, *Structural chemistry of layer-type phases*, Springer Science & Business Media, 2012.
26 J. He, S. Ma, P. Lyu and P. Nachtigall, *J. Mater. Chem. C*, 2016, **4**, 2518–2526.
27 W. B. Zhang, Q. Qu, P. Zhu and C. H. Lam, *J. Mater. Chem. C*, 2015, **3**, 12457–12468.
28 J. Liu, Q. Sun, Y. Kawazoe and P. Jena, *Phys. Chem. Chem. Phys.*, 2016, **18**, 8777–8784.
29 P. Miró, M. Audiffred and T. Heine, *Chem. Soc. Rev.*, 2014, **43**, 6537–6554.
30 P. Zhou, C. Q. Sun and L. Z. Sun, *Nano Lett.*, 2016, **16**(10), 6325–6330.
31 C. Lee, X. Wei, J. W. Kysar and J. Hone, *Science*, 2008, **321**, 385–388.
32 S. Cahangirov, M. Topsakal, E. Aktürk, H. Şahin and S. Ciraci, *Phys. Rev. Lett.*, 2009, **102**(23), 236804.
33 H. Şahin, S. Cahangirov, M. Topsakal, E. Bekaroglu, E. Akturk, R. T. Senger and S. Ciraci, *Phys. Rev. B: Condens. Matter*, 2009, **80**(15), 155453.
34 G. Henkelman, A. Arnaldsson and H. Ĵlonsson, *Comput. Mater. Sci.*, 2006, **36**, 354–360.
35 D. J. Thouless, M. Kohmoto, M. P. Nightingale and M. Den Nijs, *Phys. Rev. Lett.*, 1982, **49**, 405.
36 Y. Yao, L. Kleinman, A. H. MacDonald, J. Sinova, T. Jungwirth, D. S. Wang and Q. Niu, *Phys. Rev. Lett.*, 2004, **92**, 037204.
37 D. Xiao, M. C. Chang and Q. Niu, *Rev. Mod. Phys.*, 2010, **82**, 1959.
38 A. Rycerz, J. Tworzydło and C. W. J. Beenakker, *Nat. Phys.*, 2007, **3**, 172–175.
39 S. G. Cheng, J. Zhou, H. Jiang and Q. F. Sun, *New J. Phys.*, 2016, **18**(10), 103024.
40 T. Zhou, J. Zhang, Y. Xue, B. Zhao, H. Zhang, H. Jiang and Z. Yang, 2016, *arXiv preprint arXiv:1611.04715*.
41 G. Kresse and H. Jürgen, *Phys. Rev. B: Condens. Matter*, 1993, **47**, 558.
42 G. Kresse and D. Joubert, *Phys. Rev. B: Condens. Matter*, 1999, **59**, 1758.
43 J. P. Perdew, K. Burke and M. Ernzerhof, *Phys. Rev. Lett.*, 1996, **77**, 3865.
44 K. Parlinski, Z. Q. Li and Y. Kawazoe, *Phys. Rev. Lett.*, 1997, **78**, 4063.
45 A. Togo, F. Oba and I. Tanaka, *Phys. Rev. B: Condens. Matter*, 2008, **78**, 134106.
46 P. Giannozzi, *et al.*, *J. Phys.: Condens. Matter*, 2009, **21**, 395502 http://www.quantum-espresso.org.
47 Pseudopotentials are available at http://qe–forge.org/gf/project/pslibrary.
48 N. Marzari and D. Vanderbilt, *Phys. Rev. B: Condens. Matter*, 1997, **56**, 12847.
49 A. Mostofi, J. R. Yates, Y. S. Lee, I. Souza, D. Vanderbilt and N. Marzari, *Comput. Phys. Commun.*, 2008, **178**, 685.
50 A. A. Mostofi, J. R. Yates, G. Pizzi, Y. S. Lee, I. Souza, D. Vanderbilt and N. Marzari, *Comput. Phys. Commun.*, 2014, **185**, 2309–2310.
51 M. L. Sancho, J. L. Sancho and J. Rubio, *J. Phys. F: Met. Phys.*, 1984, **14**, 1205.

